American Mineralogist, Volume 103, pages 489–501, 2018

A Mössbauer-based XANES calibration for hydrous basalt glasses reveals radiation-induced oxidation of Fe

Elizabeth Cottrell[1,*], Antonio Lanzirotti[2], Bjorn Mysen[3], Suzanne Birner[1,4], Katherine A. Kelley[5], Roman Botcharnikov[6,7], Fred A. Davis[1,8], and Matthew Newville[2]

[1]National Museum of Natural History, Smithsonian Institution, Washington, D.C. 20560, U.S.A.
[2]University of Chicago, Chicago, Illinois 60637, U.S.A.
[3]Geophysical Laboratory, Carnegie Institution of Washington, Washington, D.C. 20015, U.S.A.
[4]Department of Geological Sciences, Stanford University, Stanford, California 94305, U.S.A.
[5]Graduate School of Oceanography, University of Rhode Island, Narragansett, Rhode Island 02882, U.S.A.
[6]Institut für Mineralogie, Leibniz Universitaet Hannover, Hannover, D-30167, Germany
[7]Institut für Geowissenschaften, Gutenberg Universitaet Mainz, Mainz, D-55128, Germany
[8]Department of Earth & Environmental Sciences, University of Minnesota Duluth, Duluth, Minnesota 55812, U.S.A.

Abstract

Oxygen fugacity (f_{O_2}) exerts first-order control on the geochemical evolution of planetary interiors, and the $Fe^{3+}/\Sigma Fe$ ratios of silicate glasses provide a useful proxy for f_{O_2}. Fe *K*-edge micro-X-ray absorption near-edge structure (XANES) spectroscopy allows researchers to micro-analytically determine the $Fe^{3+}/\Sigma Fe$ ratios of silicate glasses with high precision. In this study we characterize hydrous and anhydrous basalt glass standards with Mössbauer and XANES spectroscopy and show that synchrotron radiation causes progressive changes to the XANES spectra of hydrous glasses as a function of radiation dose (here defined as total photons delivered per square micrometer), water concentration, and initial $Fe^{3+}/\Sigma Fe$ ratio.

We report experiments from eight different radiation dose conditions and show that Fe in hydrous silicate glasses can undergo rapid oxidation upon exposure to radiation. The rate and degree of oxidation correlates with radiation dose and the product of water concentration and ferrous/ferric iron oxide ratio on a molar basis ($\Phi = X_{HO_{0.5}} \cdot X_{FeO}/X_{FeO_{1.5}}$). For example, a basalt glass with 4.9 wt% dissolved H_2O and $Fe^{3+}/\Sigma Fe = 0.19$ from its Mössbauer spectrum may appear to have $Fe^{3+}/\Sigma Fe \geq 0.35$ when analyzed over several minutes at a nominal flux density of ~2×10^9 photons/s/μm^2. This radiation-induced increase in $Fe^{3+}/\Sigma Fe$ ratio would lead to overestimation of f_{O_2} by about two orders of magnitude, with dramatic consequences for the interpretation of geological processes.

The sample area exposed to radiation shows measureable hydrogen loss, consistent with radiation-induced breaking of O–H bonds, associated H migration and loss, and oxidation of Fe^{2+}. This mechanism is consistent with the observation that anhydrous glasses show no damage under any beam conditions. Cryogenic cooling does not mitigate, but rather accelerates, iron oxidation. The effects of beam damage appear to persist indefinitely.

We detect beam damage at the lowest photon flux densities tested (3×10^6 photons/s/μm^2); however, at flux densities ≤6×10^7 photons/s/μm^2, the hydrous glass calibration curve defined by the centroid (derived from XANES spectra) and $Fe^{3+}/\Sigma Fe$ ratios (derived from Mössbauer spectra) is indistinguishable from the anhydrous calibration curve within the accuracy achievable with Mössbauer spectroscopy. Thus, published $Fe^{3+}/\Sigma Fe$ ratios from hydrous glasses measured at low photon flux densities are likely to be accurate within measurement uncertainty with respect to what would have been measured by Mössbauer spectroscopy.

These new results demonstrate that to obtain accurate $Fe^{3+}/\Sigma Fe$ ratios from hydrous, mafic, silicate glasses, it is first necessary to carefully monitor changes in the XANES spectra as a function of incident dose (e.g., fixed-energy scan). Defocusing and attenuating the beam may prevent significant oxidation of Fe in mafic water-bearing glasses.

Keywords: XANES, Mössbauer, oxygen fugacity, oxidation state, iron, glass, synchrotron radiation, hydrous basalt; Invited Centennial Article

Introduction

The $Fe^{3+}/\Sigma Fe$ ratio of silicate glass may serve as a direct proxy for the oxygen fugacity (f_{O_2}) of an igneous system, which exerts control on phase equilibria, physical properties, and the valence state of other heterovalent elements in solution (e.g., Carmichael 1991; Kress and Carmichael 1991; Sack et al. 1980). The use of Fe *K*-edge XANES to obtain $Fe^{3+}/\Sigma Fe$ ratios of hydrous silicate glasses has proliferated in recent years owing to the outstanding precision achievable and micrometer-scale spatial resolution afforded (e.g., Botcharnikov et al. 2005; Brounce et al. 2014; Cottrell and Kelley 2011; Gaetani et al. 2012; Helz et al. 2017; Kelley

* E-mail: cottrelle@si.edu

0003-004X/18/0004–489$05.00/DOI: http://doi.org/10.2138/am-2018-6268

and Cottrell 2009, 2012; Le Voyer et al. 2015; Matjuschkin et al. 2015; Moor et al. 2013; Moussallam et al. 2016; Shorttle et al. 2015; Stamper et al. 2014; Wilke et al. 2006). Most Fe-XANES calibration studies have focused on anhydrous glasses, in large part because f_{O_2} can be easily controlled in 1-atm gas-mixing furnaces (Berry et al. 2003; Cottrell et al. 2009; Dyar et al. 2016; Fiege et al. 2017; Wilke et al. 2001, 2005; Zhang et al. 2016, 2018). Given the recent surge in applications of Fe-XANES to hydrous systems, however, it is important to understand and quantify how dissolved water and radiation-induced chemical reactions may modify the spectral features used to determine $Fe^{3+}/\Sigma Fe$ ratios.

Fe-XANES pre-edge features are sensitive to the coordination environment and oxidation state of Fe (e.g., Henderson et al. 2014 and references therein). The potential effects of water dissolved in silicate glass on the structural environment of Fe are therefore of great interest to practitioners of XANES. In their Mössbauer studies on glasses, Wilke et al. (2002, 2006) observed differences in the hyperfine fields and coordination environments between hydrous and anhydrous glasses, but postulated that the differences emerged during quench. Wilke and coworkers concluded that there is no detectable influence of water on the local structural environment of Fe in melts. The effect of dissolved water on the oxidation state of Fe in melts has been the subject of more study and debate, but XANES and wet-chemical studies of mafic glasses synthesized at fixed f_{O_2} have shown water to have no effect on $Fe^{3+}/\Sigma Fe$ ratios (Botcharnikov et al. 2005; Gaillard et al. 2001; Moore et al. 1995). Given that Fe coordination affects pre-edge intensities, but not the pre-edge centroids most commonly employed to extract $Fe^{3+}/\Sigma Fe$ ratios (Bajt et al. 1994; Cottrell et al. 2009; Wilke et al. 2005), and the difficulty of independently varying f_{O_2} and f_{H_2O} in experimental systems, relatively little effort has been applied to calibrating hydrous glasses for XANES determinations of $Fe^{3+}/\Sigma Fe$ ratios.

Electron and X-ray beam interactions with materials can shift the oxidation state of various elements in biological, amorphous, and crystalline materials (e.g., Corbett et al. 2007; Eeckhout et al. 2005; Shimizugawa et al. 2001; Gonçalves Ferreira et al. 2013). For example, sulfur dissolved in silicate glass may become oxidized or reduced upon exposure to electron and X-ray beams (Klimm et al. 2012; Rowe et al. 2007; Wilke et al. 2008). Relatively little work has been done to investigate the potential effects of radiation on Fe speciation in silicate glasses. Wilke et al. (2005) and Cottrell et al. (2009) assessed, but saw no evidence for, radiation-induced beam damage in XANES spectra of anhydrous basalt glasses collected at bending magnet sources. Using an unattenuated undulator-source, Shorttle et al. (2015) assessed beam damage in glasses with <1 wt% water, and observed an increase in the intensity of the second pre-edge multiplet with time (radiation dose) that was "barely above instrument stability" (i.e., was within the noise). The study of Moussallam et al. (2016) was not able to detect beam damage by analyzing successive XANES spectra collected at a single spot on glasses with <1 wt% water at an attenuated undulator-source. However, as new radiation sources come online that can deliver higher flux densities to a sample, and studies of hydrous silicate glass proliferate, we find it prudent to examine the potential for radiation to induce beam damage.

Samples and Methods

Samples

We examine 27 glasses of basaltic composition in this study: 13 anhydrous (LW and AII) basalt glasses from the study of Cottrell et al. (2009), which are available to the community upon request to Smithsonian's National Rock Collection, and 14 hydrous (B) glasses (0.72 to 4.82 wt% dissolved total H_2O) from the study of Botcharnikov et al. (2005). For this study, all analyses were performed on double-side polished glass wafers of approximately 50–100 μm in thickness. Details of the experimental methods and complete sample characterizations can be found in Cottrell et al. (2009), Cottrell and Kelley (2011) (including wet-chemical analyses), and Botcharnikov et al. (2005).

Analytical methods

Mössbauer spectroscopy. Cottrell et al. (2009) and Botcharnikov et al. (2005) report $Fe^{3+}/\Sigma Fe$ ratios for each glass based on room-temperature Mössbauer spectroscopy, without correction for recoilless fraction. We re-report their results in Table 1, along with new results from this study for the hydrous B glasses. Method details for previously reported fits can be found in Cottrell et al. (2009) and Botcharnikov et al. (2005). Cottrell et al. (2009) applied the distribution fitting method of Alberto et al. (1996), which adopts a two-dimensional (2D) Gaussian probability distribution function for the isomer shift and quadrupole splitting. This routine minimizes the error (reduced χ^2 values) between the data and the absorption envelope that arises from the contribution of paramagnetic quadrupole doublets. The area of the fitted ferric doublet relative to the entire absorption envelope provides the $Fe^{3+}/\Sigma Fe$ ratio. Using the software package RECOIL (Lagarec and Rancourt 1998), Botcharnikov et al. (2005) applied an extended Voigt-based fitting (xVBF) method that also assumes a 2D Gaussian distribution of hyperfine parameters for ferric and ferrous iron (Lagarec and Rancourt 1997). The relative area ratios provide the $Fe^{3+}/\Sigma Fe$ ratios, and the uncertainties estimated by Botcharnikov et al. (2005) that we re-report in Table 1 reflect counting statistics, variation in the results from the application of multiple fitting models, and the possible effect of neglecting the recoilless fraction.

To isolate the effects of beam damage, deconvolution of the Mössbauer spectra for hydrous and anhydrous glasses must be consistent. Both xVBF and Alberto et al. (1996) methods fit multiple distributions (based on a Gaussian distribution of Lorentzian line shapes). The site distributions derive from maxima in the probability functions that describe the ferrous and ferric hyperfine field distributions (Mysen 2006, and references therein). Zhang et al. (2018) show that both approaches yield consistent $Fe^{3+}/\Sigma Fe$ ratios for the AII and LW glasses. To test for systematic bias between the Cottrell et al. (2009) and Botcharnikov et al. (2005) approaches, we obtained the raw spectra of Botcharnikov et al. (2005), collected at Bayerisches Geoinstitute, University of Bayreuth, and refit 14 of them using the same methods used by Cottrell et al. (2009). This ensures that our analysis of oxidative beam damage from synchrotron radiation will not be affected by inter-laboratory bias in the Mössbauer fitting protocols.

X-ray absorption near edge structure (XANES) spectroscopy. Cottrell et al. (2009) and Botcharnikov et al. (2005) report on Fe *K*-edge XANES spectra collected previously for the glasses used in this study. The former collected spectra at bending magnet station X26A at the National Synchrotron Light Source (NSLS), Brookhaven National Laboratory, New York, U.S.A., and the latter at the Hamburger Synchrotronstrahlungslabor (HASYLAB), Hamburg, Germany. Details about those facilities, collection procedures, and fitting routines can be found in Cottrell et al. (2009) and Botcharnikov et al. (2005).

For this study, we collected new Fe *K*-edge XANES spectra on the AII, LW, and B series glasses in fluorescence mode in six synchrotron beam sessions: two on bending magnet station X26A at NSLS, and four at station 13-ID-E (GSECARS) at the Advanced Photon Source (APS), Argonne National Laboratory, Illinois. We applied eight radiation dose conditions that we detail in Table 2. We cast our results in terms of radiation dose so that the results can be easily generalized to other facilities and beamline configurations. For these experiments it is more convenient and descriptive to represent the mean energy imparted to the sample in terms of flux density, rather than in the more standard SI units of Gray. However, the absorbed dose in Gray (absorption of 1 J of radiation energy per kilogram of sample) can be calculated by assuming an average basaltic glass composition and density and the depth at which the incident radiation falls to 1/e within the glass (Henke et al. 1993). For basaltic glass, the flux density is equivalent to ~75–80 times the dose in Grays/s (Table 2). As we describe below, in all sessions, and at all facilities, we set the area-weighted average energy of the pre-edge peaks (the centroid) equal to 7112.3 for anhydrous glass standard LW_0 (Cottrell et al. 2009).

LW_0 is analyzed frequently throughout all analytical sessions. Normalization of all centroids to the energy of LW_0 accounts for within-session instrumental drift in the monochromator energy calibration and for differences in monochromator calibration between facilities and between sessions (Bajt et al. 1994; Cottrell et al. 2009). The empirical drift-corrected precision (1σ) of the area-weighted centroid positions collected over a 10 year period on the AII and LW glasses is 0.004 ± 0.009 eV (n for each glass = 30–48) (Zhang et al. 2018).

We did not correct for over-absorption effects (Manceau et al. 2002). In fluorescence mode XANES, over-absorption can result in a decrease in the amplitude of the absorption peaks in samples where the absorber mass is high. This can result in a relative increase in the pre-edge peak intensities relative to the main absorption edge, but it does not impact the relative intensities of the two pre-edge peak multiplets or their energy positions (Botcharnikov et al. 2005; Cottrell et al. 2009; Zhang et al. 2016). Moreover, while over-absorption can affect pre-edge peak intensities, all glass compositions examined here have sufficiently high total FeO contents (7–12 wt%) and thicknesses (>50 μm) to be in the infinite thickness regime.

X26A, NSLS, Brookhaven National Laboratory, U.S.A. NSLS (decommissioned in October, 2014) operated at 2.8 GeV and 300 mA. We collected fluorescence spectra on the B series glasses at bending magnet beamline X26A using summed energy-dispersive spectra from a 4-element Vortex ME-4 silicon drift diode detector and two single element Vortex-EX detectors (Hitachi) with pulse processing provided by an XMap digital spectrometer system (XIA). The first derivative of Fe *K*-edge spectra (E_0) collected on zero-valent Fe E_0 is 7112.0 eV. All other methods details are as reported by Cottrell et al. (2009). The incident beam flux at X26A was consistently ~3×10^9 photons/s and the spot size was 9 × 5 μm such that the photon flux density was ~6.7×10^7 photons/s/μm^2 (Table 2); after a 15.5 min collection the absorbed dose per spectrum was ~6×10^{10} photons/μm^2.

13-ID-E, GSECARS, Advanced Photon Source, Argonne National Laboratory, U.S.A. Details regarding the beamline configuration for 13-ID-E can be found in Sutton et al. (2017). This undulator-based beamline at APS operates at 7 GeV and 85–101 mA. We collected fluorescence spectra with a Vortex ME4 silicon-drift diode detector array coupled to a high-speed digital spectrometer system (Quantum Xpress3). A cryogenically cooled double-crystal Si (311) monochromator provided the monochromatic radiation. The first derivative of Fe *K*-edge spectra (E_0) collected on zero-valent Fe E_0 is 7110.75 eV. We collected spectra from 7012 to 7102 eV in 2.5 eV steps with 1 s dwell; from 7102 to 7132 eV (pre-edge region) in 0.1 eV steps with 1 s dwell and from 7132 to 7492 eV (XAFS region) in 2.3 Å steps with 1 s dwell. We edge-step normalized the spectra collected at 13-ID-E by the average intensity between 7315 and 7320 eV where the spectra were flat.

The 13-ID-E beamline is capable of delivering and detecting in excess of 1×10^{12} photons/s within a focused spot size of 2 × 2 μm at the Fe *K*-edge, so that focused flux densities of ~5×10^{11} photons/s/μm^2 are possible—four orders of magnitude higher than what was possible at X26A. We collected the experimental data presented here over a ~10^4 range in flux density to precisely assess the spectral response to absorbed radiation dose. At 13-ID-E we collected spectra using six protocols where incident flux density was adjusted, through upstream aperturing of the X-ray beam, through filtering using varying thicknesses of aluminum foil, and through defocusing of the incident beam on the sample. These conditions are reported in Table 2.

We also conducted one set of analyses at 13-ID-E under cryogenic conditions, using a customized cryogenic stage described in Tappero et al. (2016, 2017), to investigate the degree to which cryogenic cooling may mitigate the observed iron oxidation. We collected a time series at an energy of 7113.3 eV at both ambient and cryogenic conditions reported in Table 2.

TABLE 1. Mössbauer $Fe^{3+}/\Sigma Fe$ ratios, and select compositional parameters

Sample	$Fe^{3+}/\Sigma Fe \cdot 100$		Botcharnikov et al. (2005)		Φ[a]
	Botcharnikov et al. (2005) (1σ)	This study (1σ)	FeO Total wt%	H_2O Total wt%	
B11	19(2)	18.7(1.45)	12.49	4.82	1.05
B16	18(2)	16.8(1.23)	12.93	3.02	0.81
B12	11(2)	12.3(1.81)	12.02	1.9	0.77
B13	10(2)	12(1.41)	11.39	1.71	0.72
B10	40(4)	36.3(1.61)	12.61	2.43	0.24
B6	39(3)	36.9(1.72)	12.94	2	0.19
B9	29(3)	26.7(2.14)	12.62	1.14	0.19
B7	23(2)	21.1(0.94)	12.91	0.97	0.22
B8	16(2)	17.8(1.15)	12.67	0.82	0.23
B17	60(2)	55.6(2.03)	12.65	4.67	0.19
B21	49(2)	45.7(1.53)	12.34	2.9	0.19
B19	52(2)	49.3(1.68)	12.91	1.85	0.11
B22	28(2)	25.3(0.38)	12.77	0.94	0.17
B20	25(2)	24.8(1.00)	12.80	0.72	0.13
		Cottrell et al. 2009 (1σ)[b]			
AII_0	–	14.7(0.38)			
AII_-05	–	19.4(0.63)			
AII_05	–	13.8(0.50)			
AII_15	–	24.7(0.44)			
AII_-15	–	9.3(0.60)			
AII_25	–	35.6(0.38)			
AII_35	–	48.4(0.40)			
AII_45	–	61.1(0.26)			
LW_0	–	16.2(0.55)			
LW_10	–	23.5(0.53)			
LW_-10	–	13(0.58)			
LW_20	–	30.3(0.14)			
LW_-20	–	8.8(0.53)			

[a] $\Phi = X_{HO_{0.5}} \cdot X_{FeO}/X_{FeO_{1.5}}$ based on $Fe^{3+}/\Sigma Fe$ ratios from this study and H_2O from Botcharnikov et al. (2005).
[b] From room-temperature spectra. New recommended values, considering recoiless fraction, can be found in Zhang et al. (2018).

Fourier transform infrared (FTIR) spectroscopy

Glass chip B10 (Table 1) was analyzed by FTIR for dissolved total H_2O using a Thermo-Nicolet iS50 FTIR bench spectrometer coupled with a Continuum IR microscope with automated mapping capability at the Graduate School of Oceanography, University of Rhode Island. We mapped an area on a chip of B10 that had been purposely exposed to high photon flux at beamline 13-ID-E. The map was collected using transmission FTIR with a 20 × 20 μm square aperture and no overlap between pixels. Each spectrum was collected over 1200–6000 cm^{-1} wavenumbers using 256 scans at 1 cm^{-1} resolution. Individual transmission spectra were reduced for H_2O^{Total} after fitting the spectral background with a spline function and calculating the net intensity of the absorbance band at 3500 cm^{-1}. The H_2O^{Total} concentration was then calculated using the Beer-Lambert law, a calculated density of 2.90 g/cm^3, thickness of 49 ± 1 μm, and the molar absorption coefficient $\varepsilon^{3530} = 63$, which is assumed constant within the compositional range of basalts (Dixon et al. 1995).

RESULTS

Mössbauer spectra

Mössbauer-derived $Fe^{3+}/\Sigma Fe$ ratios are not very sensitive to fitting philosophy or method, but in this study we re-fit the B glass spectra acquired by Botcharnikov et al. (2005) to eliminate any potential bias between the disparate fitting routines of Cottrell et al. (2009) and Botcharnikov et al. (2005). In addition, our new fits

TABLE 2. Synchrotron radiation dose conditions

Flux condition	Spot size (μm)	Photon flux (photons/s)	Flux (photons/s/μm^2)	Gray/s[a] density	Notes
$XANES_1$	2 × 2	$5 \times 10^{10–11}$	$1 \times 10^{10–11}$	$9.0 \times 10^{10–11}$	nominal at 13-ID-E
$XANES_3$	2 × 2	$1.5–8.6 \times 10^9$	4×10^8 to 2×10^9	~1.3×10^7	
$XANES_4$	50 × 50	$1.5–8.6 \times 10^9$	8×10^5 to 3×10^6	~1.3×10^4	
$XANES_5$	25 × 25	2×10^9	3×10^6	3.8×10^4	
$XANES_{CRYO-HI}$	38 × 28	$3–4 \times 10^7$	$3–4 \times 10^4$		monochrometer = 7113.3 eV
$XANES_{CRYO-LO}$	38 × 28	$2–4 \times 10^6$	$2–4 \times 10^3$		monochrometer = 7113.3 eV
X26A	9 × 5	3×10^9	6×10^7	7.7×10^5	

[a] Dose in Gray (J/kg/s) is calculated for glass of basaltic composition through 1/e absorption length.

allow us to report hyperfine parameters for these glasses that may aid in understanding the structural environment of Fe in hydrous and anhydrous glasses. We provide the Mössbauer spectra from Botcharnikov et al. (2005) and our fits from this study (spectra, fits, hyperfine parameters, and plots) in the Supplementary Material[1].

Two quadrupole doublets, one ferric with a low isomer shift (IS) of 0.4 to 0.6 mm/s (relative to Fe metal) and low quadrupole splitting (QS) of 0.8 to 1.1 mm/s, and one ferrous with a high isomer shift of 0.8 to 1.0 mm/s and quadrupole splitting of 1.9 to 2.2 mm/s, describe the Mössbauer spectra of the B glasses (Supplementary Material; Supplemental[1] Figs. S1 and S2). The Botcharnikov et al. (2005) study did not report hyperfine parameters, but the hyperfine parameters derived from the glass spectra in this study are similar to those reported previously in the literature for silicate glasses (Alberto et al. 1996; Jayasuriya et al. 2004; Mysen et al. 1985a; Zhang et al. 2016). Ferrous iron IS and QS in the hydrous B glasses are within error of those for the anhydrous glasses for all but the most highly oxidized glasses, for which the quadrupole splitting in the hydrous glasses is higher. The QS for ferric iron is smaller in hydrous glasses than in anhydrous glasses by approximately 0.25 to 0.45 mm/s. The IS of ferric iron is slightly higher in the hydrous glasses than in the anhydrous glasses, and tends to decrease with increasing $Fe^{3+}/\Sigma Fe$ ratio, as expected (Mysen and Richet 2005; Mysen and Virgo 1989; Mysen 2006). While many factors influence the coordination of ferric iron in silicate glasses (Mysen and Richet 2005), the greater ferric IS observed in the hydrous glasses suggests that the O–Fe^{3+} bond length is longer, and weaker (e.g., Johnson et al. 1999), and that ferric iron is in higher average coordination (greater domination of $^{VI}Fe^{3+}$) in the hydrous B glasses than in the anhydrous AII and LW glasses. Higher coordination of ferric iron in the hydrous glasses is consistent with results from (Wilke et al. 2002, 2006), and is corroborated by XANES spectra, as we discuss below.

The $Fe^{3+}/\Sigma Fe$ ratios in the B glasses, as determined by the new fits reported here, range from 0.12 to 0.56, compared to 0.10 to 0.60 for those same glasses reported in Botcharnikov et al. (2005). The $Fe^{3+}/\Sigma Fe$ ratios of all B glasses with nominal $Fe^{3+}/\Sigma Fe < 0.50$ agreed within 1σ (2.7% absolute) with the values reported by Botcharnikov et al. (2005). The three glasses with $Fe^{3+}/\Sigma Fe$ ratios > 0.50 agreed within 2σ of the uncertainties on the fits (4.4% absolute). These fits are within the commonly accepted uncertainty of the technique, which ranges from ±1 to 6% in absolute $Fe^{3+}/\Sigma Fe$ ratio (Dyar et al. 1987; Mysen et al. 1985a, 1985b). $Fe^{3+}/\Sigma Fe$ ratios from the Botcharnikov et al. (2005) study correlate very well with ratios obtained in this study ($R^2 > 0.99$, m = 0.9, b = 1.87). Consistent with the results of Cottrell et al. (2009), Zhang et al. (2015), and Zhang et al. (2018), inclusion of a second ferrous doublet in the present study did not reduce the χ^2 of the fits.

XANES

Bending magnet beamlines, X26A NSLS. Full XANES spectra of hydrous B and anhydrous AII and LW glasses collected at bending magnet beamline X26A are shown in Figure 1. We provide spectra for AII and LW anhydrous glasses from a 2014 NSLS session for reference (there is no substantive change since their initial publication in Cottrell et al. 2009). As demonstrated by Botcharnikov et al. (2005) for previous XANES analyses of the B glasses, the energy of the main absorption edge, the ratio of pre-edge peak intensities, and the area-weighted average energy of the pre-edge peaks (the centroid) in the XANES spectra shift smoothly as a function of $Fe^{3+}/\Sigma Fe$ ratio (e.g., Berry et al. 2003; Botcharnikov et al. 2005; Cottrell et al. 2009; Wilke et al. 2001, 2005). The shift in centroid energy provides a precise proxy for $Fe^{3+}/\Sigma Fe$ ratio in basaltic glasses, especially for $Fe^{3+}/\Sigma Fe$ ratios below 0.50 (Henderson et al. 2014). We report the centroids and pre-edge peak intensities for all glasses in Table 3. We provide all fitting parameters in Supplemental[1] Table S2. Consistent with the results of Cottrell et al. (2009), centroids obtained from spatially independent spectra are precise to ≤ ±0.01 eV.

For anhydrous LW and AII glasses and hydrous B glasses, we plot the $Fe^{3+}/\Sigma Fe$ ratios derived from Mössbauer fits determined by Botcharnikov et al. (2005) and this study against the $Fe^{3+}/\Sigma Fe$ ratios derived from XANES at low flux using the anhydrous calibration curve of Cottrell et al. (2009). Regardless of which set of Mössbauer values are used, the $Fe^{3+}/\Sigma Fe$ ratios of the hydrous glasses fall within 1σ of a 1:1 relationship (Fig. 2a).

Undulator-based beamlines, 13-ID-E, APS. Full XANES spectra of AII, LW, and B glasses collected at insertion device beamline 13-ID-E (GSECARS) are shown in Figure 1 and we provide fitting parameters in Supplemental[1] Table S2.

Condition $XANES_1$, anhydrous glasses. We report centroids (area weighted average energy of the two pre-edge multiplets) under "nominal" operating conditions at 13-ID-E, our condition "$XANES_1$," for each glass in Table 3.

Under normal high flux operating conditions at station 13-1D-E, we recover the $Fe^{3+}/\Sigma Fe$ ratios of anhydrous glasses when we use the calibration of Cottrell et al. (2009), which was developed at low flux. Anhydrous glass $Fe^{3+}/\Sigma Fe$ ratios derived from XANES at high flux fall within 1σ of a 1:1 relationship with the Mössbauer-derived values (Fig. 2b). Supplemental[1] Figure S3a and Table 3 show that high-flux centroids are on average within ±0.008eV (within 1σ) of low-flux centroids. One might conclude from this that the centroid, as a spectral feature, is a robust proxy for assessment of the $Fe^{3+}/\Sigma Fe$ ratio for anhydrous glasses. We emphasize again, however, the importance of normalizing to a standard. While the centroids at the two facilities are reproducible, the individual spectral features are not. Differences in modeled spectral features (Supplemental[1] Figs. S3b, S3c, and S3d) and the raw spectra (Supplemental[1] Fig. S4) reflect the smaller vertical emittance of the 13-ID-E undulator electron beam compared to the X26A bending magnet source, and the optical configuration at each beamline. That we reproduce the centroids of anhydrous glasses across facilities to approximately ±0.01 eV is a non-trivial result. Fiege et al. (2017) state that the "overall uncertainty" in the centroid is an order of magnitude higher (±0.1 eV). We attribute the high precision we achieve primarily to ensuring that we account for instrumental drift within and between analytical sessions by shifting the energy of all centroids such that the centroid of LW_0 ≡ 7112.3 eV. The key result is that the anhydrous glass centroids remain stable within uncertainty at all beam conditions and across all facilities.

Condition $XANES_1$, hydrous glasses. At a given $Fe^{3+}/\Sigma Fe$ ratio, the centroids of hydrous B glasses are variably shifted to higher values at 13-ID-E under nominal operating conditions

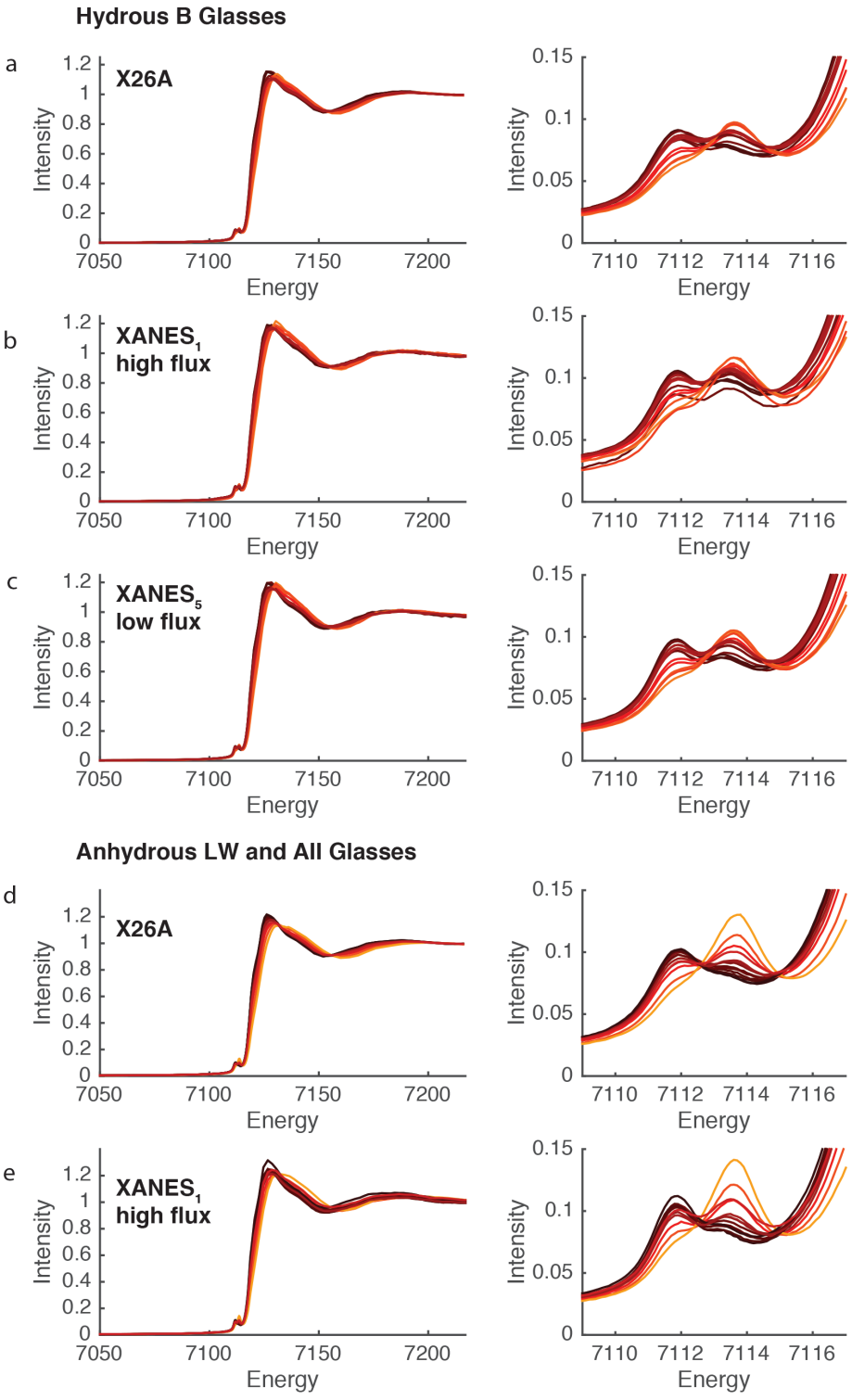

FIGURE 1. XANES spectra for hydrous B glasses and anhydrous LW and AII glasses under three radiation dose conditions. Left-hand panels show full spectra; right-hand panels magnify the pre-edge region. Spectra are color-coded by relative $Fe^{3+}/\Sigma Fe$ ratio as determined by Mössbauer spectroscopy (black are the most reduced glasses, grading through red and orange to yellow, which are the most oxidized glasses). Note the smooth, monotonic, decrease in the intensity in the first pre-edge multiplet and increase in intensity of the second pre-edge multiplet as a function of $Fe^{3+}/\Sigma Fe$ ratio for the hydrous samples under the bending magnet and low radiation dose conditions, and the anhydrous glasses under all dose conditions. Spectra of hydrous B glasses under the high radiation dose condition do not evolve systematically as a function of $Fe^{3+}/\Sigma Fe$ ratio.

TABLE 3. XANES centroids and integrated pre-edge intensities

	X26A[a] 5×10^{10} photons/μm²				$XANES_1$ 3×10^{15} photons/μm²				$XANES_5$ 2×10^{9} photons/μm²				
Sample	Centroid	σ	I1	I2	Centroid	σ	I1	I2	Centroid	σ	I1	I2	%Δ[b]
B11	7112.402	0.012	0.06	0.037	7112.654	0.015	0.053	0.066	7112.421	0.003	0.058	0.045	71.9
B16	7112.342	0.008	0.063	0.031	7112.578	0.007	0.057	0.057	7112.362	0.01	0.061	0.04	69.2
B12	7112.226	0.007	0.073	0.026	7112.4	0.016	0.07	0.046	7112.228	0.002	0.074	0.032	66.4
B13	7112.177	0.002	0.077	0.024	7112.328	0.011	0.073	0.038	7112.211	0.015	0.076	0.031	46.0
B10	7112.784	0.01	0.047	0.062	7112.86	0.018	0.045	0.082	7112.773	0.004	0.048	0.074	18.4
B6	7112.733	0.012	0.05	0.06	7112.793	0.017	0.049	0.076	7112.735	0.007	0.052	0.07	6.5
B9	7112.585	0.006	0.06	0.05	7112.633	0.006	0.06	0.066	7112.568	0.011	0.06	0.058	16.5
B7	7112.477	0.007	0.064	0.042	7112.505	0.009	0.066	0.054	7112.468	0.009	0.064	0.05	18.7
B8	7112.413	0.007	0.07	0.04	7112.451	0.026	0.066	0.05	7112.418	0.006	0.067	0.047	27.2
B17	7113.083	0.013	0.03	0.088	7113.108	0.016	0.029	0.106	7113.059	0.001	0.032	0.098	3.8
B21	7112.988	0.006	0.039	0.082	7113.029	0.014	0.039	0.104	7112.957	0.008	0.04	0.088	15.5
B19	7113.01	0.008	0.04	0.083	7112.99	0.011	0.042	0.097	7112.969	0.008	0.042	0.094	2.3
B22	7112.587	0.01	0.062	0.051	7112.613	0.008	0.06	0.064	7112.582	0.01	0.06	0.06	19.1
B20	7112.548	0.002	0.064	0.048	7112.551	0.009	0.064	0.058	7112.538	0.009	0.063	0.057	9.5
	5×10^{10} photons/μm²				4×10^{15} photons/μm²								
All_0	7112.275	0.01	0.091	0.03	7112.271	0.009	0.079	0.036					
All_05	7112.361	0.011	0.086	0.038	7112.368	0.002	0.08	0.046					
All_-05	7112.219	0.01	0.09	0.029	7112.22	0.004	0.084	0.034					
All_15	7112.52	0.013	0.078	0.047	7112.529	0.002	0.069	0.058					
All_-15	7112.147	0.026	0.093	0.02	7112.134	0.007	0.087	0.025					
All_25	7112.742	0.014	0.068	0.07	7112.76	0.009	0.061	0.079					
All_35	7112.962	0.027	0.055	0.091	7112.974	0.002	0.052	0.106					
All_45	7113.184	0.025	0.046	0.124	7113.186	0.003	0.042	0.14					
LW_0	7112.3	0.01	0.085	0.032	7112.302	0.01	0.079	0.04					
LW_10	7112.434	0.013	0.078	0.042	7112.433	0.009	0.07	0.05					
LW_-10	7112.154	0.024	0.095	0.023	7112.155	0.004	0.085	0.028					
LW_20	7112.608	0.02	0.072	0.058	7112.62	0.002	0.069	0.069					
LW_-20	7112.112	0.01	0.097	0.018	7112.128	0.002	0.092	0.027					

Note: Doses reported in this table are per spectrum (photons/s/μm² × total collection time).
[a] Centroids of All and LW glasses are 7 year averages (n = 30–48) as reported in Zhang et al. (2018).
[b] $(Fe^{3+}/\Sigma Fe_{Möss} - Fe^{3+}/\Sigma Fe_{XANES})/Fe^{3+}/\Sigma FeMöss \cdot 100$.

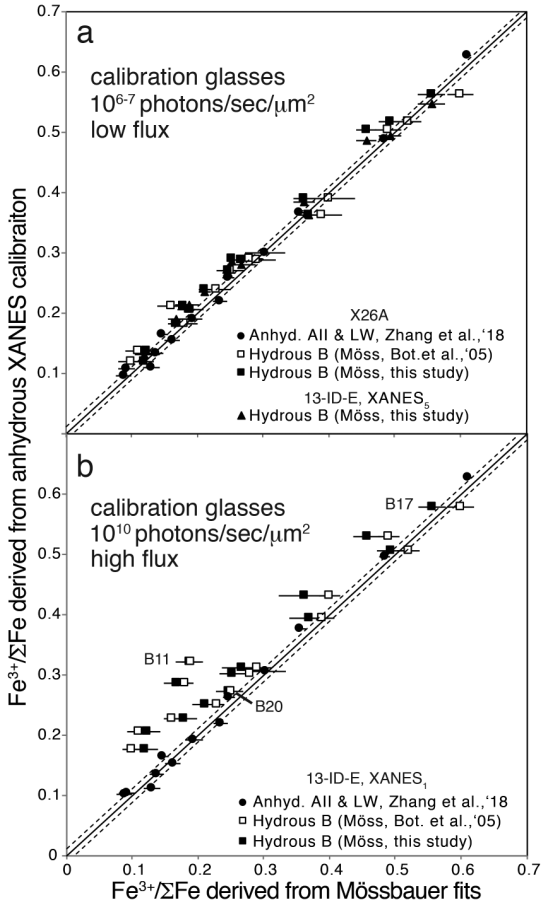

◀**FIGURE 2.** (**a**) $Fe^{3+}/\Sigma Fe$ ratios determined by Mössbauer spectroscopy vs. $Fe^{3+}/\Sigma Fe$ ratios determined by XANES (average of three spatially independent spots per sample) at a flux of 10^{6-7} photons/s/μm² using the anhydrous basalt calibration curve of Cottrell et al. (2009). Filled circles = anhydrous basalts, Cottrell et al. (2009). Open squares = hydrous basalts, Botcharnikov et al. (2005). Filled squares and filled triangles = hydrous basalts, this study. The anhydrous basalts, on which this calibration is based, fall slightly off the 1:1 line because we have used the average centroid of these glasses collected over a 10 yr period (n = 30–48 per glass) as reported in Zhang et al. (2018) to highlight the reproducibility of the measurement. (**b**) The same analysis as in **a**, but at a higher flux of 10^{10} photons/s/μm². Vertical 1σ error bars are smaller than the symbol sizes. Horizontal 1σ error bars are the errors on the Mössbauer determinations. Dashed lines show the predictive capability of the model using a leave-one-out cross validation method (Arlot and Celisse 2010). The root mean square uncertainty for the predicted $Fe^{3+}/\Sigma Fe$ ratios of unknowns determined from the basaltic calibration is <±0.01 (1σ).

($XANES_1$), in stark contrast to the highly reproducible anhydrous glasses (Table 3). For some hydrous glasses (e.g., B20), we derive the same centroid within 0.003 eV (within 1σ) between facilities, but for others (e.g., B11) we derive a centroid up to 0.25 eV higher (25σ higher) under high-flux conditions than low-flux conditions (Supplemental[1] Fig. S5). This manifests as XANES-derived $Fe^{3+}/\Sigma Fe$ ratios that are up to 1.7 times higher than those derived from Mössbauer spectroscopy (Fig. 2b).

Intensity of second multiplet with time. To better evaluate how the Fe XANES spectra of these glasses evolve with accumulated radiation dose, we conducted experiments to monitor changes in the intensity of the second pre-edge multiplet at 7113.3 eV (attributed to Fe^{3+}) as a function of time and flux density (i.e., dose). Glass B11 was used for this experiment; it is the most

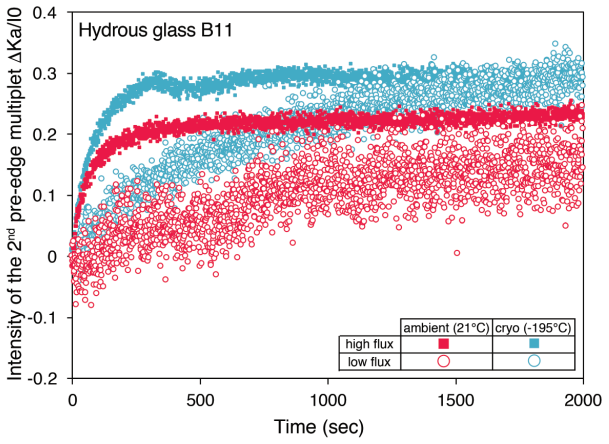

FIGURE 3. Time-dependence of the intensity of the second pre-edge multiplet (ΔFe$K\alpha$/IO) during exposure to synchrotron radiation under four beam conditions: high flux density (filled squares) and low flux density (open circles); and at ambient temperature (red) and with the sample cryogenically cooled to –195 °C (blue). The intensity of the second pre-edge multiplet is higher (i.e., more radiation-induced oxidative beam damage) when the sample is cryogenically cooled under both beam conditions.

hydrous in the suite under study, with 4.82 wt% total dissolved water, and $Fe^{3+}/\Sigma Fe = 0.19$.

Figure 3 plots the peak amplitude of the second pre-edge multiplet peak of hydrous glass B11 with time, measured at high-flux and low-flux density under both ambient and cryogenically cooled conditions. We first consider data collected at ambient temperature. Peak amplitude increases with time under high- and low-flux conditions, with a rapid increase observed within the first 100 s of high flux irradiation. The higher photon flux density generated by the focused beam causes a greater increase in the amplitude of the second pre-edge multiplet at all time points. However, when the change in amplitude is measured relative to the dose delivered, the amplitude of the second multiplet (extent of damage) increases at approximately the same rate in high- and low-flux density conditions. This evidences the dose-dependence of the spectral change. While low flux beam damage does not affect the centroid of these hydrous glasses within the measurement error of our calibration (Fig. 2; Supplemental[1] Fig. S5), these data show that damage occurs in hydrous glasses even at low-flux density.

We then explored the degree to which cryogenic cooling impacts spectral evolution with time. Studies over a broad range of incident beam energies show that cryo-cooling of biological samples significantly reduces damage due to mass (water) loss during exposure to ionizing radiation (e.g., Dubochet et al. 1988; Steinbrecht and Zierold 2012). Cryo-cooling may also potentially reduce the rate of beam-induced changes in metal valence state in some materials (Corbett et al. 2007; Grabolle et al. 2006), although the degree to which this mitigates the effects is debated (Beetz and Jacobsen 2003; Meents et al. 2010). We repeated the time series experiments described previously on sample B11, with the glass held at –195 °C. The measurements show the surprising result that at cryogenic temperatures, under both high- and low-flux density conditions, the relative rate of Fe oxidation increases. Beam damage is worse at cryogenic temperatures.

It is also instructive to see that spectral changes plateau under all conditions studied within 3–16 min. It takes anywhere from approximately 4 to 30 min to collect an entire quality XANES spectrum on glass with FeO concentrations between 5 and 10 wt% (e.g., Cottrell and Kelley 2011; Shorttle et al. 2015). Therefore, successive XANES spectra, collected at a single sample position, may not show any measurable change if damage begins to plateau before acquisition of the first spectrum is finished.

Conditions $XANES_{3,4}$ successive analysis at one position. Using glass B11 again, we show in Figure 4a and Supplemental[1] Table S3 how the centroids of successive analyses on the same spot in glass B11 increase if we employ condition $XANES_4$, a very low flux achieved by attenuating and defocusing the beam to 50 × 50 μm. The centroid increases approximately logarithmically in energy for each successive spectrum. Contrast this with succes-

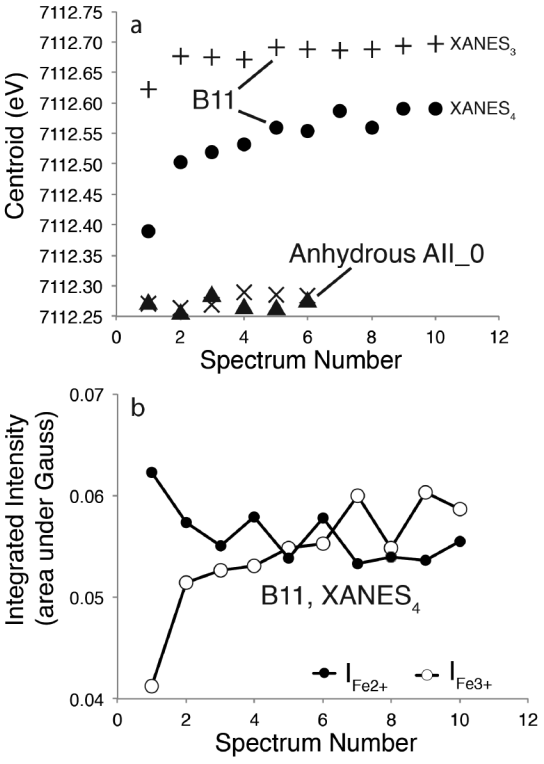

FIGURE 4. Evolution of spectral features as a function of spectrum number (proxy for dose) for spectra acquired in succession in the same position on the sample for hydrous glass B11 and anhydrous glass AII_0. (**a**) Evolution of centroids under two beam conditions, high radiation dose condition $XANES_3$ ("+" and "x" symbols) and low radiation dose condition $XANES_4$ (circles and triangles). Centroids of successive spots on anhydrous glass AII_0 show no significant changes under either beam condition. Application of a high radiation dose, typical of focused beams at undulator beamlines, does not result in significant changes to the centroids of successive spectra on the same spot of hydrous glass B11; however, centroids acquired using a high radiation dose are higher than centroids collected on the same sample at low radiation dose. Significant increases in the centroids of successive spots on hydrous glass B11 only become apparent using a low radiation dose. Vertical 1σ error bars are smaller than the symbol sizes. (**b**) Evolution of $I_{Fe^{2+}}$ and $I_{Fe^{3+}}$ with successive spectra taken at the same position under low radiation dose condition $XANES_4$. Vertical 1σ error bars are smaller than the symbol sizes.

sive spots at the same incident flux, but with the beam focused to 2 × 2 μm ($XANES_3$), in which case the total number of photons delivered to a given area (photons/μm^2) is higher after just one spectral acquisition than after successive analyses under condition $XANES_4$. The centroid is commensurately higher, and plateaus after one acquisition. Figure 4b reveals how the integrated intensity (area) of the Gaussian extracted for the first multiplet ($I_{Fe^{2+}}$) decreases while the integrated intensity of the second multiplet ($I_{Fe^{3+}}$) increases. Evolution of the spectra in this manner is consistent with oxidation of Fe^{2+} to Fe^{3+}. Consistent with Cottrell et al. (2009), we observe no change in the centroid or pre-edge peak intensities with successive analyses on anhydrous glass AII_0.

Observations of the raw spectra (Fig. 5) confirm the spectral evolution seen in the modeled parameters. Raw spectra collected sequentially at a given position on sample B11, under condition $XANES_4$, show decreases in the intensity of the first pre-edge multiplet and increases in intensity of the second pre-edge multiplet. In addition, we see the main absorption edge move to higher energy as radiation dose accumulates. Spectral changes are consistent with an increase in the average oxidation state of Fe with increasing radiation dose.

Beam damage persists indefinitely

To assess the longevity of beam damage, we mapped glass B11 approximately one year after a session in which we investigated beam damage. In Figure 6, image brightness scales with the ratio between the Fe$K\alpha$ fluorescence peak amplitude at 7113.2 eV, the energy maximum for the Fe^{3+} pre-edge multiplet peak, and at 7111.6 eV, the energy maximum for the Fe^{2+} pre-edge multiplet peak. In the false-color inset, the bright white areas correspond to previously analyzed spots. From this map it is evident that areas exposed to high radiation dose retain higher Fe^{3+}/Fe^{2+} ratios than adjacent areas that were not exposed to the X-ray beam at least one year after exposure. Beam damage persists indefinitely.

Coordination of Fe in hydrous and anhydrous glasses

Figure 7 compares the summed integrated pre-edge intensities (areas) ($I_{Fe^{2+}} + I_{Fe^{3+}}$) of hydrous and anhydrous glasses as a function of their centroids—what Wilke et al. (2001) coined a "variogram." Because $I_{Fe^{2+}}$ and $I_{Fe^{3+}}$ are extremely sensitive to detector dead time, edge-step normalization procedure, self-absorption, etc., they are generally not comparable between facilities and are even difficult to compare between analytical sessions at the same facility (Cottrell et al. 2009). We only compare spectra acquired at APS in Figure 7; these have been collected and processed under conditions as uniform as can be practically achieved.

All glasses display typical pre-edge intensities indicative of fivefold or mixed fourfold and sixfold coordination (Wilke et al. 2001, 2005). We see that hydrous glasses fall along the same trend of increasing integrated pre-edge intensity with centroid energy under both the high flux density condition $XANES_3$ and the low-flux density condition $XANES_4$. Covariation in the oxidation state and coordination of Fe in these glasses is consistent with a shift in Fe coordination upon exposure to radiation only in proportion to the shift in Fe oxidation state. This analysis therefore also points to actual oxidation of Fe^{2+} to Fe^{3+} in the hydrous glasses.

The variogram also corroborates the site geometry analysis of the Mössbauer spectra, which revealed higher Fe^{3+} isomer shift (and smaller quadrupole splitting) in hydrous B glasses relative to anhydrous glasses (Supplemental[1] Fig. S2), consistent with longer, weaker, O–Fe^{3+} bonds, and Fe^{3+} in higher coordination in the hydrous glasses than the anhydrous AII and LW glasses. In Figure 7, anhydrous glasses display higher integrated intensities (lower average coordination) than hydrous glasses at any given centroid energy, consistent with longer and weaker O–Fe^{3+} bonds in the hydrous glasses. Correcting for over-absorption does not change this relationship.

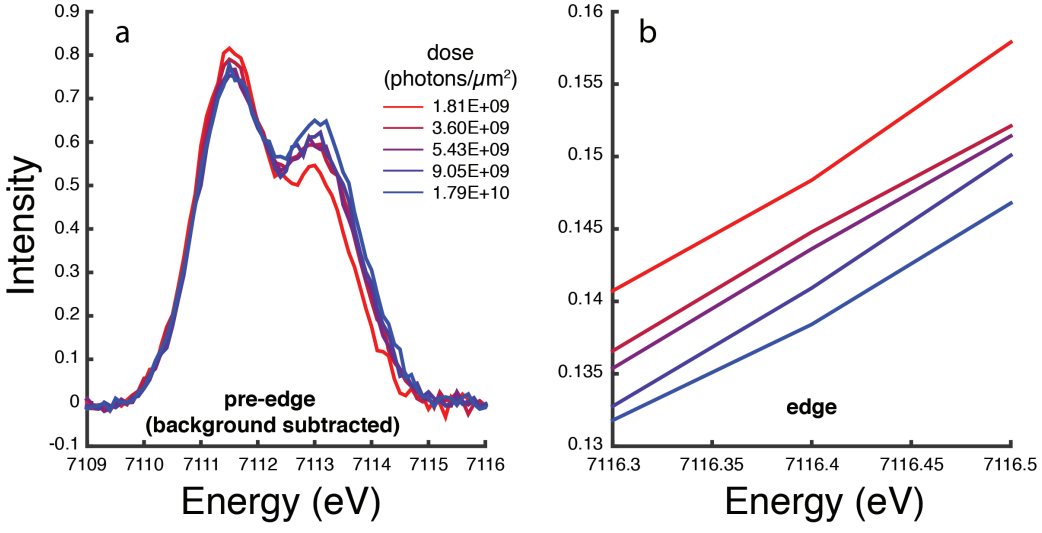

Figure 5. (**a**) Evolution the background-subtracted pre-edge, acquired via successive analyses in the same sample position, as a function of radiation dose, using condition $XANES_4$. As the total dose increases, the intensity of the first pre-edge multiplet decreases while the second increases. (**b**) The main edge moves to progressively higher energy as dose increases.

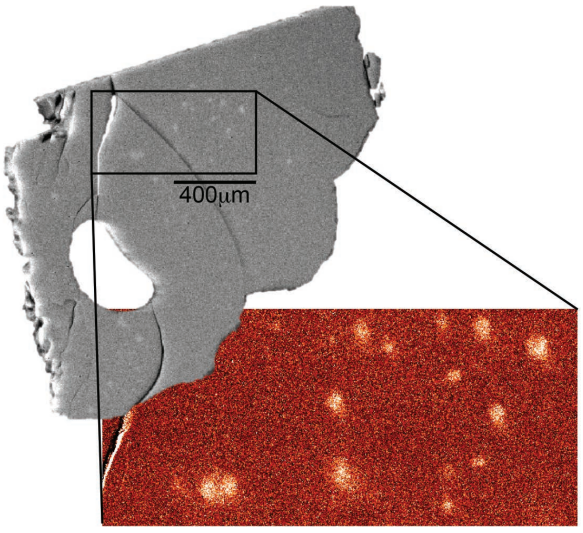

FIGURE 6. The grayscale image is a peak amplitude map collected at ~7113.2 eV (energy of second pre-edge multiplet) of hydrous glass B11. Image color is scaled to maximum intensity, where white is high and black is low. The inset map is a peak amplitude map collected at 7113.2/7111.6eV (peak amplitude of the second pre-edge multiplet divided by the peak amplitude of the first pre-edge multiplet). Image color is scaled to maximum peak amplitude, where white is high and red is low. White areas show spots analyzed >1 yr earlier.

DISCUSSION

The 1*s* absorption edge and pre-edge peaks in 3*d* transition metals, like Fe, are due to electron transitions from 1*s* to 3*d* states (e.g., Henderson et al. 2014). Quadrupole (1*s*3*d*) and dipole (1*s* to the 4*p* character of the 3*d* band) transitions are possible in silicate glasses, owing to iron's mixed coordination. In XANES spectra, Fe^{2+} exhibits 2 or 3 pre-edge peaks, and Fe^{3+} exhibits 1 or 2 pre-edge peaks, depending on coordination (Westre et al. 1997). $I_{Fe^{2+}}$ and $I_{Fe^{3+}}$ increase as coordination number decreases (i.e., with higher extents of 3*d* + 4*p* mixing) because of the added dipole contribution (Roe et al. 1984; Westre et al. 1997). The relative integrated intensities and energies of the pre-edge peaks therefore depend on the metal site geometry: the relative proportions of Fe^{2+} and Fe^{3+} and their coordination as tetrahedral (fourfold) or octahedral (sixfold) (Henderson et al. 2014; Wilke et al. 2001). Thus, it is necessary to evaluate the degree to which the observed beam-induced changes in the XANES spectra reflect changes in effective Fe valence as compared to coordination, particularly since in glasses these effects are coupled.

We considered the possibility that exposure to radiation in hydrous glasses, but not anhydrous glasses, might increase 3*d*-4*p* hybridization of Fe^{3+} centers. For example, Fe^{3+}–OH^- bonds could respond differently to radiation than Fe^{3+}–O bonds. Augmented hybridization of Fe^{3+} centers in hydrous glasses would increase the dipole contribution to the second multiplet, increase its integrated intensity, and increase the centroid, without any change in the actual average oxidation state of Fe. Yet, several lines of evidence argue against this possibility. First, upon exposure to a high photon flux density, the XANES spectra of the hydrous glasses show that the Fe^{3+} multiplet integrated intensity increases and the Fe^{2+} multiplet intensity concomitantly decreases (Fig. 4). Moreover, the white line shifts to progressively higher energy as well (Fig. 5). These three spectral changes together are much more consistent with oxidation of Fe^{2+} to Fe^{3+} than an increase in 3*d*-4*p* hybridization, as the latter would result in neither a decrease in the intensity of the first multiplet, nor a shift in the main edge.

Because no measurable change in the XANES spectra is observed as a function of dose in spectra collected from anhydrous glasses (e.g., Figs. 2 and 4), we hypothesize that the changes we observe in the spectra of hydrous B glasses with exposure to ionizing radiation relates to their dissolved water contents. Here we use $Fe^{3+}/\Sigma Fe_{Möss}$–$Fe^{3+}/\Sigma Fe_{XANES}$ as a proxy for beam-induced Fe oxidation, where Mössbauer spectra establish the "true" $Fe^{3+}/\Sigma Fe$ ratio, and the XANES centroid the "apparent" $Fe^{3+}/\Sigma Fe$ ratio

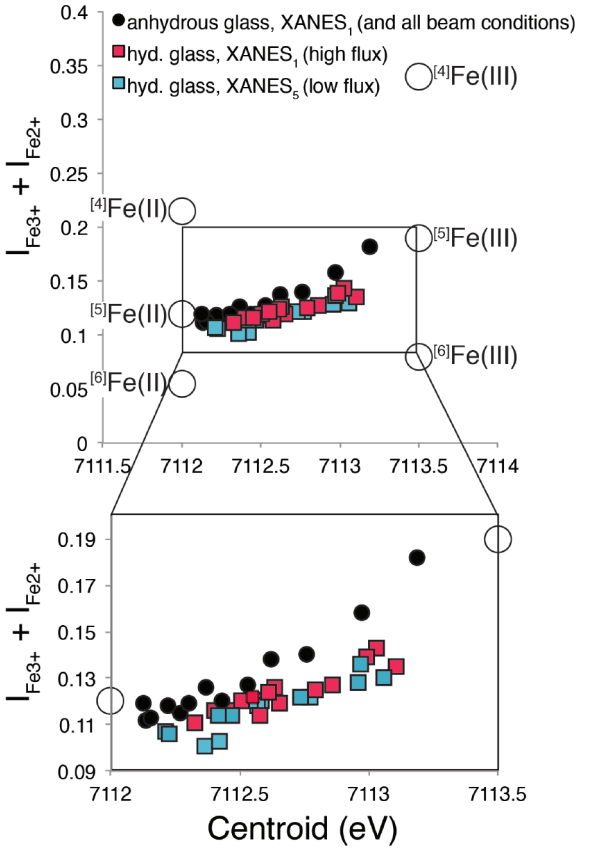

FIGURE 7. A "variogram" showing the spectral characteristics of centroid vs. integrated pre-edge intensity (area) of Fe in end-member structural environments (large empty circles) from Wilke et al. (2001) and glasses from this study. Anhydrous (black circles) and hydrous glass (red and blue squares) spectral characteristics from this study are consistent with iron in fivefold coordination or a mixture of fourfold and sixfold coordination. Under the same radiation dose conditions, anhydrous glasses display higher pre-edge intensities relative to hydrous glasses at a given centroid energy. Hydrous glasses under high radiation dose conditions display higher pre-edge intensities than under low radiation dose conditions; however, increases in pre-edge intensities are proportional to increases in the centroid ($Fe^{3+}/\Sigma Fe$ ratio). Vertical 1σ error bars are smaller than the symbol sizes.

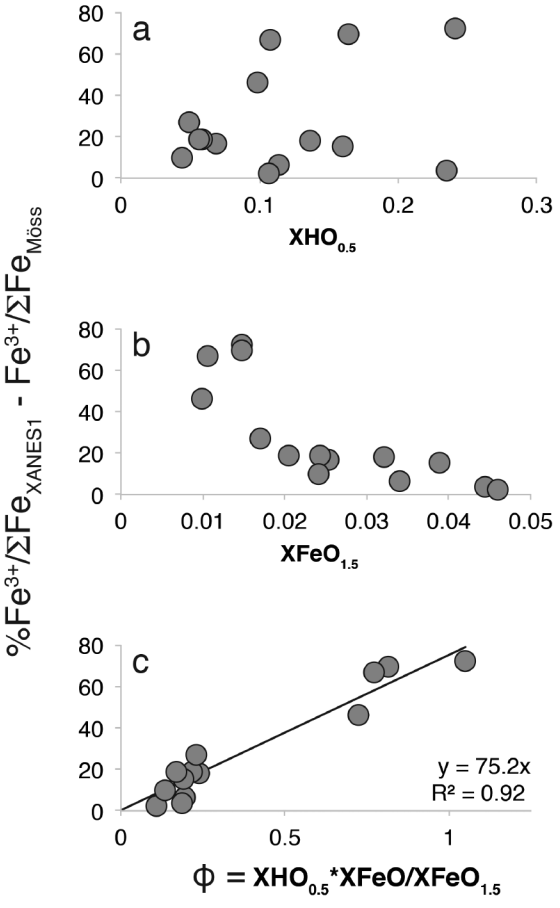

FIGURE 8. We use $Fe^{3+}/\Sigma Fe_{Möss} - Fe^{3+}/\Sigma Fe_{XANES}$ as a proxy for beam-induced Fe oxidation (where Mössbauer spectra establish the "true" $Fe^{3+}/\Sigma Fe$ ratio, and the XANES centroid the "apparent" $Fe^{3+}/\Sigma Fe$ ratio). Here we plot the molar concentration of (**a**) dissolved water (single cation basis), $X_{HO_{0.5}}$, (**b**) ferric iron (single cation basis), $X_{FeO_{1.5}}$, and (**c**) the ratio of dissolved water multipled by the ferrous/ferric ratio, $\Phi = X_{HO_{0.5}} \cdot X_{FeO}/X_{FeO_{1.5}}$, vs. $\%Fe^{3+}/\Sigma Fe_{Möss} - Fe^{3+}/\Sigma Fe_{XANES}$. The correlation in **c** is forced through the origin, because we observe no oxidative beam damage in anhydrous glasses. 1σ error bars are smaller than the symbol sizes.

(Table 3). Indeed, when we compare glass B8 to B16, glasses of similar $Fe^{3+}/\Sigma Fe$ ratio, we see that the centroid of glass B16, with >3.6 times more dissolved water, is overestimated by ~70%, whereas the centroid of glass B8 is overestimated by ~27% when exposed to the same radiation dose. Figure 8a shows, however, that total dissolved H_2O in the glasses does not correlate with beam-induced Fe oxidation. For example, the anhydrous XANES calibration of Cottrell et al. (2009) predicts the $Fe^{3+}/\Sigma Fe$ ratio of hydrous glass B17, with 4.67 wt% total water, within error of its "true" value, while the centroid of B11, with nearly indistinguishable dissolved water content, is overestimated by >70% (Figs. 4 and 9). The latter overestimation of $Fe^{3+}/\Sigma Fe$ ratio leads to overestimation of f_{O_2} by two orders of magnitude.

Following this, it is also clear that when the initial oxidation state of Fe is high, the spectral response to radiation (beam damage) is lessened (Fig. 8b). Upon exposure to the same high photon dose (condition $XANES_1$), the $Fe^{3+}/\Sigma Fe$ ratios of hydrous glasses with lower $Fe^{3+}/\Sigma Fe$ ratios are greatly overestimated in comparison to glasses with higher $Fe^{3+}/\Sigma Fe$ ratios (R^2 linear correlation = 0.53; R^2 exponential correlation = 0.72, Fig. 8b).

All the evidence suggests to us that the mechanism of Fe oxidation involves breaking of O–H bonds by incident ionizing radiation, loss of hydrogen, and concomitant oxidation of Fe^{2+} to Fe^{3+}. One possible reaction, analogous to that proposed for radiation-induced oxidation of S dissolved in hydrous silicate glasses by Klimm et al. (2012) is:

$$H_2O + 2Fe^{2+}O \rightarrow H^{\uparrow}_{2(gas?)} + Fe^{3+}_2O_3.$$

The loss of hydrogen gas is consistent with the longevity of the beam damage, as discussed above and shown in Figure 6. This mechanism is also consistent with the observed dependence on both the initial $Fe^{3+}/\Sigma Fe$ ratio and the dissolved water content of the hydrous glass.

The hypothesized mechanism suggests that a fruitful metric for predicting the susceptibility of hydrous glass to beam damage is the molar ratio of dissolved total water to the ferric/ferrous ratio as determined by Mössbauer spectroscopy ($\Phi = XHO_{0.5} \cdot XFeO/XFeO_{1.5}$ ratio) (Table 1). We find that beam damage susceptibility, Φ, correlates strongly with the extent to which high photon flux $XANES_1$ overestimates the $Fe^{3+}/\Sigma Fe$ ratio ($R^2 = 0.92$, n = 14, b ≡ 0 because anhydrous glasses show no damage) (Fig. 8c).

Inspection of the raw spectra of the B glasses under conditions $XANES_3$ and $XANES_4$ confirms that spectral changes increase as a function of dose and increasing Φ, with anhydrous glasses showing no spectral change (Fig. 9). Visual inspection also verifies that the spectral features all evolve in a manner consistent with oxidation of ferrous iron to ferric iron: $I_{Fe^{2+}}$ falls; $I_{Fe^{3+}}$ grows; and the *K* edge shifts to higher energy. Spectral changes increase in proportion to Φ. We provide the spectra for Figure 9 in Supplemental[1] Table S4.

We tested this hypothesis by subjecting glass B10 to a 2 × 2 μm beam of high photon flux of ~1×10^{12} photons/s for ~12 min (Fig. 10). We subsequently mapped the area surrounding this spot on the sample via Fourier transform infrared spectroscopy (FTIR). The FTIR data show that the area of the glass adjacent to the exposed spot (e.g., pixel 1, Fig. 10) has significantly lower dissolved H_2O than areas of the glass distant from exposure (e.g., pixel 2, Fig. 10). We reduced individual FTIR spectra from pixels 1 and 2 by fitting the background of the total H_2O absorption band at 3500 cm^{-1} with a spline function that was then subtracted from the spectra before measuring the band height. This analysis shows that pixel 2, away from the potential damage zone, has a total dissolved H_2O content of 2.43 wt%, which is identical to the reported H_2O content for this glass by Botcharnikov et al. (2005). The dissolved H_2O content of pixel 1, however, is 900 ppm lower (2.34 wt%). Pixel 1 is not coincident with the location of the XANES beam at the sample surface. Rather, the incident X-ray beam intersects the sample surface at a 45° angle relative to the FTIR incident beam, which is normal to the sample surface. The high flux X-ray beam traveled through the sample, from right to left in Figure 10, at 45° angle, and thus interacted with the glass chip to the left of the beam cross-hair location. We

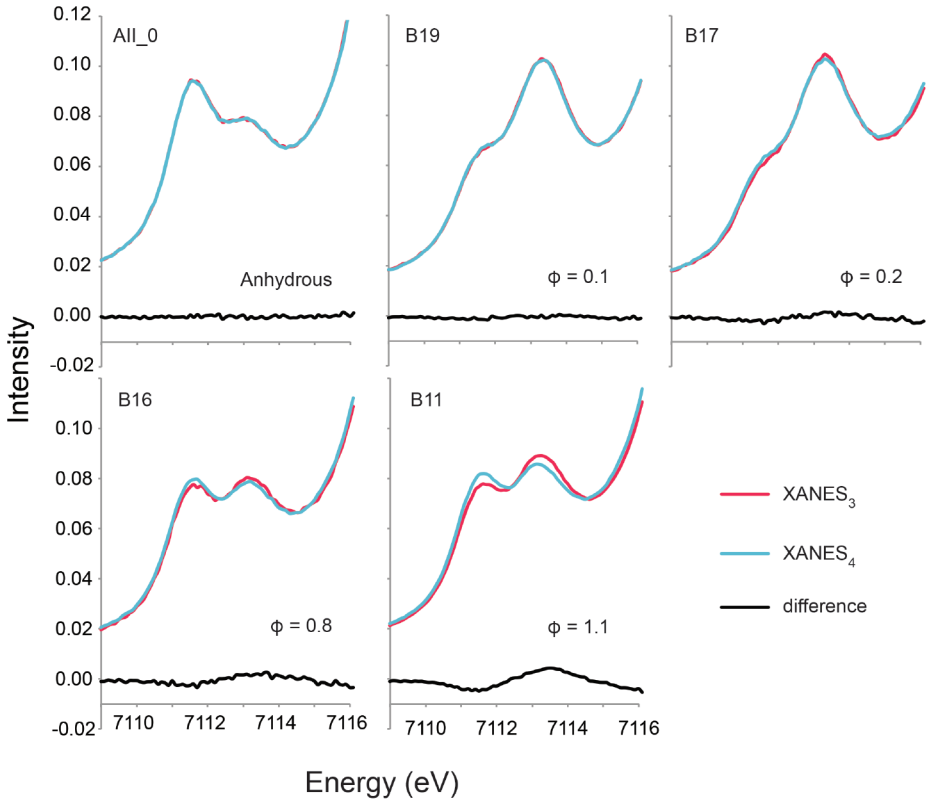

FIGURE 9. Pre-edge spectra of one anhydrous and four hydrous glasses, with varying Φ and under two radiation dose conditions. We display merged, successive spectra, acquired under two different beam conditions: high radiation dose condition $XANES_3$ (red) and low radiation dose condition $XANES_4$ (blue). The black line shows the difference between the spectra.

conclude from this assessment that exposure of this sample to a high-flux XANES beam caused both oxidation of Fe and water loss from the glass, which supports the proposed mechanism of Fe oxidation via hydrogen loss. We note that only a few percent of the Fe fluorescence we measure comes from the sample surface. The geometrical considerations we present above and the magnitude of the spectral changes and water loss we observe require chemical changes to the bulk affected volume. Damage cannot be limited to the sample surface.

Cryo-cooling has been shown to mitigate beam damage (e.g., Steinbrecht and Zierold 2012; Corbett et al. 2007). Our finding that cryo-cooling exacerbated Fe^{2+} oxidation in hydrous glass is an important and counterintuitive observation. We have shown that hydrogen concentrations in the glass are lower in areas that have experienced oxidizing beam damage, consistent with radiation-induced breaking of O–H bonds, and preferential diffusion of hydrogen, relative to oxygen, away from the area. Because it is the relative diffusivity of hydrogen and oxygen that matters, and diffusivity depends strongly on temperature, we speculate that oxygen is able to diffuse farther from the analyzed spot in the room-temperature case than the cryo-cooled case (whereas hydrogen is always able to diffuse away). This may be why cryo-cooling is counterproductive when attempting to mitigate radiation-induced oxidation of Fe in hydrous silicate glass. Indeed, Gonçalves Ferreira et al. (2013) found that heating soda-lime glasses to 500 °C actually mitigated radiation-induced *reduction* of iron, emphasizing that the effect of temperature on beam damage will depend on the nature and mechanism of beam damage and is difficult to predict a priori.

IMPLICATIONS

Prior XANES studies of hydrous glasses

We have shown that synchrotron radiation causes progressive changes to the XANES spectra of hydrous glasses, but not anhydrous glasses, as a function of radiation dose. Spectral changes are consistent with preferential migration of hydrogen relative to oxygen, and oxidation of iron, in the analysis spot. Our study reveals that oxidative beam damage occurs in hydrous glasses even at the lowest flux densities achieved, but that damage is not detectable outside of the error of anhydrous calibrations with exposure to radiation doses typically found at bending magnet sources. Conversely, it would be prudent to re-evaluate results from studies carried out on hydrous glasses at undulator beam lines using a focused spot.

Mafic glasses may be synthesized experimentally with a wide range of Φ ($XHO_{0.5}{\cdot}XFeO/XFeO_{1.5}$) that may readily exceed those investigated in this study. Most naturally occurring basaltic glasses, however, will have $0 < \Phi < 1$. For example, basaltic glass inclusions in volcanic rocks from subduction zones have Φ ranging from ~0.34 to ~1; natural basaltic glasses from sea floor volcanoes erupting in back arc basins have ratios ranging from ~0.2 to ~0.6; and mid-ocean ridge basalts have ratios between ~0.05 to ~0.28 (ranges estimated from data in Brounce et al. 2014; Cottrell and Kelley 2011; Kelley and Cottrell 2012). Based on the work presented here, all submarine basalts and undegassed melt inclusions would suffer significant beam damage under nominal acquisition conditions (i.e., a focused beam) at unattenuated undulator beam lines. We have also shown, however, that a radiation

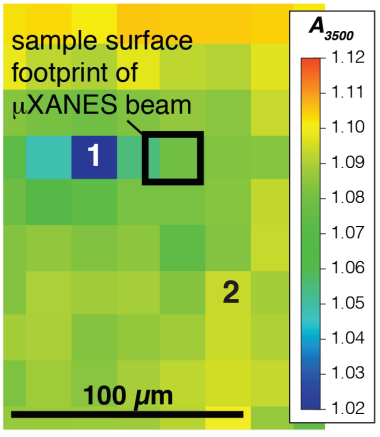

FIGURE 10. FTIR transmission map of glass B10 surrounding an area purposely exposed with a 2 × 2 μm synchrotron radiation beam at a photon flux of ~1 × 10^{12} photons/s for ~12 min. We show the location of the beam at the sample surface, but the beam intersects the sample surface at a 45° angle and travels through the sample from right to left. Color scale shows the intensity of the H_2O_{total} absorbance band at 3500 cm^{-1} after subtraction of a reference intensity at 2300 cm^{-1}. Each pixel is 20 × 20 μm. FTIR spectra for pixels designated 1 and 2 are discussed in the text.

dose of ≤6 × 10^7 photons/s/μm^2 mitigates (but does not prevent) beam damage on hydrous glasses with Φ up to ~1.

We hypothesize that damage may not have been detected in previous studies conducted at high dose conditions because, under nominal operating conditions, radiation damage is maximum or "complete" after acquisition of a single spectrum (~600 s for spectra acquired under condition $XANES_1$). Collection of multiple spectra at a single position on the glass under condition $XANES_1$ will therefore return the same centroid because damage is complete ("saturated") before the pre-edge is scanned the first time. For materials with relatively low Φ, it may be sufficient at an undulator source to attenuate the beam to prevent beam damage from exceeding detection limits (e.g., Shorttle et al. 2015). We have shown here, however, that even at the lowest fluxes achievable at 13-ID-E, attenuation is insufficient to prevent beam damage; the beam must also be defocused.

Recommended analytical protocols for acquisition of Fe-XANES spectra on hydrous glasses

Synchrotron radiation causes progressive changes to the XANES spectra of hydrous glasses as a function of radiation dose and Φ. Dose is a function of photon flux, beam diameter, and exposure time, and can/should be calculated and reported for any synchrotron experiment. Attenuating the beam, defocusing the spot, or both, may mitigate beam damage. Using a cryostat is unlikely to mitigate beam damage; it may even exacerbate damage. This study suggests that a radiation dose of ≤6 × 10^7 photons/s/μm^2 will allow the centroids of most terrestrial basalts to lie within analytical error of anhydrous calibration curves. We emphasize that beam damage must be assessed at each beamline and for the specific materials under analysis in a given study.

ACKNOWLEDGMENTS

With admiration, we thank Catherine McCammon, who graciously provided her raw Mössbauer spectra and laboratory notes to E.C. We thank Tim Gooding for laboratory support at Smithsonian. E.C. gratefully acknowledges support from NSF EAR 1347248, NSF EAR 1426717, and NSF OCE 1433212. S.K.B. was further supported by OCE-1434199/OCE-1620276. K.K. gratefully acknowledges support from NSF EAR 1347330 and NSF OCE 1433182. We are grateful for support from Smithsonian's Scholarly Studies program. F.D. also acknowledges support from a National Museum of Natural History Peter Buck Fellowship. We are grateful for support for X26A from Department of Energy (DOE) GeoSciences DE-FG02-92ER14244. The DOE Office of Science supported use of the NSLS under contract no. DE-AC02-98CH10886. We acknowledge the support of GeoSoilEnviroCARS (Sector 13), which is supported by the National Science Foundation—Earth Sciences (EAR-1128799), and the Department of Energy, Geosciences (DE-FG02-94ER14466). This research used resources of the Advanced Photon Source, a U.S. Department of Energy (DOE) Office of Science User Facility operated for the DOE Office of Science by Argonne National Laboratory under contract no. DE-AC02-06CH11357. We thank editorial handling by Sasa Bajt and Keith Putirka as well as two anonymous reviewers for constructive comments that improved the submission.

REFERENCES CITED

Alberto, H.V., Pinto da Cunha, J.L., Mysen, B.O., Gil, J.M., and Ayres de Campos, N. (1996) Analysis of Mossbauer spectra of silicate glasses using a two-dimensional Gaussian distribution of hyperfine parameters. Journal of Non-Crystalline Solids, 194, 48–57.

Arlot, S., and Celisse, A. (2010) A survey of cross-validation procedures for model selection. Statistics Surveys, 4, 40–79.

Bajt, S., Sutton, S.R., and Delaney, J.S. (1994) X-ray microprobe analysis of iron oxidation-states in silicates and oxides using X-ray-absorption near-edge structure (XANES). Geochimica et Cosmochimica Acta, 58(23), 5209–5214.

Beetz, T., and Jacobsen, C. (2003) Soft X-ray radiation-damage studies in PMMA using a cryo-STXM. Journal of Synchrotron Radiation, 10(3), 280–283.

Berry, A.J., O'Neill, H.St.C., Jayasuriya, K.D., Campbell, S.J., and Foran, G.J. (2003) XANES calibrations for the oxidation state of iron in a silicate glass. American Mineralogist, 88(7), 967–977.

Botcharnikov, R.E., Koepke, J., Holtz, F., McCammon, C., and Wilke, M. (2005) The effect of water activity on the oxidation and structural state of Fe in a ferro-basaltic melt. Geochimica et Cosmochimica Acta, 69(21), 5071–5085.

Brounce, M., Kelley, K., and Cottrell, E. (2014) Variations in $Fe^{3+}/\Sigma Fe$ of Mariana arc basalts and mantle wedge f_{O_2}. Journal of Petrology, 55(12), 2513–2536.

Carmichael, I.S.E. (1991) The redox states of basic and silicic magmas—a reflection of their source regions. Contributions to Mineralogy and Petrology, 106(2), 129–141.

Corbett, M.C., Latimer, M.J., Poulos, T.L., Sevrioukova, I.F., Hodgson, K.O., and Hedman, B. (2007) Photoreduction of the active site of the metalloprotein putidaredoxin by synchrotron radiation. Acta Crystallographica, D63(9), 951–960.

Cottrell, E., and Kelley, K.A. (2011) The oxidation state of Fe in MORB glasses and the oxygen fugacity of the upper mantle. Earth and Planetary Science Letters, 305(3-4), 270–282.

Cottrell, E., Kelley, K.A., Lanzirotti, A., and Fischer, R.A. (2009) High-precision determination of iron oxidation state in silicate glasses using XANES. Chemical Geology, 268(3-4), 167–179.

Dixon, J.E., Stolper, E.M., and Holloway, J.R. (1995) An experimental study of water and carbon dioxide solubilities in mid ocean ridge basaltic liquids.1. Calibration and solubility models. Journal of Petrology, 36(6), 1607–1631.

Dubochet, J., Adrian, M., Chang, J.-J., Homo, J.-C., Lepault, J., McDowall, A.W., and Schultz, P. (1988) Cryo-electron microscopy of vitrified specimens. Quarterly Reviews of Biophysics, 21(2), 129–228.

Dyar, M.D., Naney, M.T., and Swanson, S.E. (1987) Effects of quench methods on Fe^{3+}/Fe^{2+} ratios—a Mössbauer and wet-chemical study. American Mineralogist, 72(7-8), 792–800.

Dyar, M.D., Breves, E.A., Gunter, M.E., Lanzirotti, A., Tucker, J.M., Carey, C., Peel, S.E., Brown, E.B., Oberti, R., and Lerotic, M. (2016) Use of multivariate analysis for synchrotron micro-XANES analysis of iron valence state in amphiboles. American Mineralogist, 101(5), 1171–1189.

Eeckhout, S.G., Neisius, T., and Castañeda, C. (2005) Oxidation effects in beryl induced by synchrotron radiation. Nuclear Instruments and Methods in Physics Research Section B: Beam Interactions with Materials and Atoms, 229(1), 73–77.

Fiege, A., Ruprecht, P., Simon, A.C., Bell, A.S., Göttlicher, J., Newville, M., Lanzirotti, T., and Moore, G. (2017) Calibration of Fe XANES for high-precision determination of Fe oxidation state in glasses: Comparison of new and existing results obtained at different synchrotron radiation sources. American Mineralogist, 102(2), 369–380.

Gaetani, G.A., O'Leary, J.A., Shimizu, N., Bucholz, C.E., and Newville, M. (2012) Rapid reequilibration of H_2O and oxygen fugacity in olivine-hosted melt inclusions. Geology, 40(10), 915–918.

Gaillard, F., Scaillet, B., Pichavant, M., and Beny, J.L. (2001) The effect of water and f_{O_2} on the ferric-ferrous ratio of silicic melts. Chemical Geology, 174(1-3),

255–273.
Gonçalves Ferreira, P., de Ligny, D., Lazzari, O., Jean, A., Cintora Gonzalez, O., and Neuville, D.R. (2013) Photoreduction of iron by a synchrotron X-ray beam in low iron content soda-lime silicate glasses. Chemical Geology, 346, 106–112.
Grabolle, M., Haumann, M., Müller, C., Liebisch, P., and Dau, H. (2006) Rapid loss of structural motifs in the manganese complex of oxygenic photosynthesis by X-ray irradiation at 10–300 K. Journal of Biological Chemistry, 281(8), 4580–4588.
Helz, R., Cottrell, E., Brounce, M., and Kelley, K. (2017) Olivine-melt relationships and syneruptive redox variations in the 1959 eruption of Kīlauea Volcano as revealed by XANES. Journal of Volcanology and Geothermal Research, 333, 1–14.
Henderson, G.S., de Groot, F.M.F., and Moulton, B.J.A. (2014) X-ray absorption near-edge structure (XANES) spectroscopy. Reviews in Mineralogy and Geochemistry, 78(1), 75–138.
Henke, B.L., Gullikson, E.M., and Davis, J.C. (1993) X-ray interactions: photoabsorption, scattering, transmission, and reflection at E = 50-30,000 eV, Z = 1-92. Atomic Data and Nuclear Data Tables, 54(2), 181–342.
Jayasuriya, K.D., O'Neill, H.St.C., Berry, A.J., and Campbell, S.J. (2004) A Mössbauer study of the oxidation state of Fe in silicate melts. American Mineralogist, 89(11-12), 1597–1609.
Johnson, J., Johnson, C., Holland, D., Mekki, A., Appleyard, P., and Thomas, M. (1999) Transition metal ions in ternary sodium silicate glasses: a Mössbauer and neutron study. Journal of Non-Crystalline Solids, 246(1), 104–114.
Kelley, K.A., and Cottrell, E. (2009) Water and the oxidation state of subduction zone magmas. Science, 325(5940), 605–607.
——— (2012) The influence of magmatic differentiation on the oxidation state of Fe in a basaltic arc magma. Earth and Planetary Science Letters, 329, 109–121.
Klimm, K., Kohn, S.C., O'Dell, L.A., Botcharnikov, R.E., and Smith, M.E. (2012) The dissolution mechanism of sulphur in hydrous silicate melts. I: Assessment of analytical techniques in determining the sulphur speciation in iron-free to iron-poor glasses. Chemical Geology, 322-323, 237–249.
Kress, V.C., and Carmichael, I.S.E. (1991) The compressibility of silicate liquids containing Fe_2O_3 and the effect of composition, temperature, oxygen fugacity and pressure on their redox states. Contributions to Mineralogy and Petrology, 108, 82–92.
Lagarec, K., and Rancourt, D. (1997) Extended Voigt-based analytic lineshape method for determining N-dimensional correlated hyperfine parameter distributions in Mössbauer spectroscopy. Nuclear Instruments and Methods in Physics Research Section B: Beam Interactions with Materials and Atoms, 129(2), 266–280.
——— (1998) RECOIL, Mössbauer spectral analysis software for windows (version 1.0). Department of Physics, University of Ottawa, Canada.
Le Voyer, M., Cottrell, E., Kelley, K.A., Brounce, M., and Hauri, E.H. (2015) The effect of primary versus secondary processes on the volatile content of MORB glasses: An example from the equatorial Mid-Atlantic Ridge (5° N–3° S). Journal of Geophysical Research: Solid Earth, 120(1), 125–144.
Matjuschkin, V., Brooker, R.A., Tattitch, B., Blundy, J.D., and Stamper, C.C. (2015) Control and monitoring of oxygen fugacity in piston cylinder experiments. Contributions to Mineralogy and Petrology, 169(1), 1–16.
Manceau, A., Marcus, M.A., and Tamura, N. (2002) Quantitative speciation of heavy metals in soils and sediments by synchrotron X-ray techniques. Reviews in Mineralogy and Geochemistry, 49(1), 341–428.
Meents, A., Gutmann, S., Wagner, A., and Schulze-Briese, C. (2010) Origin and temperature dependence of radiation damage in biological samples at cryogenic temperatures. Proceedings of the National Academy of Sciences, 107(3), 1094–1099.
Moor, J., Fischer, T., Sharp, Z., King, P., Wilke, M., Botcharnikov, R., Cottrell, E., Zelenski, M., Marty, B., and Klimm, K. (2013) Sulfur degassing at Erta Ale (Ethiopia) and Masaya (Nicaragua) volcanoes: Implications for degassing processes and oxygen fugacities of basaltic systems. Geochemistry, Geophysics, Geosystems, 14(10), 4076–4108.
Moore, G., Righter, K., and Carmichael, I.S.E. (1995) The effect of dissolved water on the oxidation-state of iron in natural silicate liquids. Contributions to Mineralogy and Petrology, 120(2), 170–179.
Moussallam, Y., Edmonds, M., Scaillet, B., Peters, N., Gennaro, E., Sides, I., and Oppenheimer, C. (2016) The impact of degassing on the oxidation state of basaltic magmas: A case study of Kīlauea volcano. Earth and Planetary Science Letters, 450, 317–325.
Mysen, B.O. (2006) Redox equilibria of iron and silicate melt structure: Implications for olivine/melt element partitioning. Geochimica et Cosmochimica Acta, 70(12), 3121–3138.
Mysen, B.O., and Richet, P. (2005) Silicate Glasses and Melts—Properties and Structure, 548 p. Elsevier, New York.
Mysen, B.O., and Virgo, D. (1989) Redox equilibria, structure, and properties of Fe-bearing aluminosilicate melts: Relationships between temperature, composition, and oxyen fugacity in the system Na_2O-Al_2O_3-SiO_2-FeO. American Mineralogist, 74, 58–76.
Mysen, B.O., Carmichael, I.S.E., and Virgo, D. (1985a) A comparison of iron redox ratios in silicate-glasses determined by wet-chemical and ^{57}Fe Mossbauer resonant absorption methods. Contributions to Mineralogy and Petrology, 90(2-3), 101–106.
Mysen, B.O., Virgo, D., Neumann, E.R., and Seifert, F.A. (1985b) Redox equilibria and the structural states of ferric and ferrous iron in melts in the system Ca-Mg-Al_3-Si_2-Fe—Relationships between redox equilibria, melt structure and liquidus phase-equilibria. American Mineralogist, 70(3-4), 317–331.
Roe, A., Schneider, D., Mayer, R., Pyrz, J., Widom, J., and Que, L. Jr. (1984) X-ray absorption spectroscopy of iron-tyrosinate proteins. Journal of the American Chemical Society, 106(6), 1676–1681.
Rowe, M.C., Kent, A.J.R., and Nielsen, R.L. (2007) Determination of sulfur speciation and oxidation state of olivine hosted melt inclusions. Chemical Geology, 236(3-4), 303–322.
Sack, R.O., Carmichael, I.S.E., Rivers, M., and Ghiorso, M.S. (1980) Ferric-ferrous equilibria in natural silicate liquids at 1 bar. Contributions to Mineralogy and Petrology, 75(4), 369–376.
Shimizugawa, J., Umesaki, M., Hanada, M., Sakai, M., and Qiu, M. (2001) X-ray induced reduction of rare earth ion doped in Na_2O-Al_2O_3-B_2O_3 glasses. Journal of Synchrotron Radiation, 8(2), 797–799.
Shorttle, O., Moussallam, Y., Hartley, M.E., Maclennan, J., Edmonds, M., and Murton, B.J. (2015) Fe-XANES analyses of Reykjanes Ridge basalts: Implications for oceanic crust's role in the solid Earth oxygen cycle. Earth and Planetary Science Letters, 427, 272–285.
Stamper, C., Melekhova, E., Blundy, J., Arculus, R., Humphreys, M., and Brooker, R. (2014) Oxidised phase relations of a primitive basalt from Grenada, Lesser Antilles. Contributions to Mineralogy and Petrology, 167(1), 954.
Steinbrecht, R.A., and Zierold, K. (2012) Cryotechniques in biological electron microscopy. Springer.
Sutton, S.R., Lanzirotti, A., Newville, M., Rivers, M.L., Eng, P., and Lefticariu, L. (2017) Spatially resolved elemental analysis, spectroscopy and diffraction at the GSECARS Sector at the Advanced Photon Source. Journal of Environment Quality, 46(6), 1158–1165.
Tappero, R., Smith, R.J., Acerbo, A.S., DiFabio, J., and Miller, L. (2016) Can cryo-cooling mitigate chemical changes for hydrated samples? International Conference on X-ray Microscopy, Abstract no. 0014.
Tappero, R., Smith, R.J., Acerbo, A.S., Lanzirotti, A., Newville, M., Sutton, S.R., Northrup, P., O'Hara, S., and Miller, L.M. (2017) A portable cryostage system for X-ray fluorescence microprobes. 14th International Conference on the Biogeochemistry of Trace Elements (ICOBTE).
Westre, T.A., Kennepohl, P., DeWitt, J.G., Hedman, B., Hodgson, K.O., and Solomon, E.I. (1997) A multiplet analysis of Fe K-edge 1s → 3d pre-edge features of iron complexes. Journal of American Chemical Society, 119, 6297–6314.
Wilke, M., Farges, F., Petit, P.-E., Brown, G.E. Jr., and Martin, F. (2001) Oxidation state and coordination of Fe in minerals: An Fe K-XANES spectroscopic study. American Mineralogist, 86(5-6), 714–730.
Wilke, M., Behrens, H., Burkhard, D.J.M., and Rossano, S. (2002) The oxidation state of iron in silicic melt at 500 MPa water pressure. Chemical Geology, 189(1-2), 55–67.
Wilke, M., Partzsch, G.M., Bernhardt, R., and Lattard, D. (2005) Determination of the iron oxidation state in basaltic glasses using XANES at the K-edge. Chemical Geology, 220(1-2), 143–161.
Wilke, M., Schmidt, C., Farges, F., Malavergne, V., Gautron, L., Simionovici, A., Hahn, M., and Petit, P.E. (2006) Structural environment of iron in hydrous aluminosilicate glass and melt-evidence from X-ray absorption spectroscopy. Chemical Geology, 229(1-3), 144–161.
Wilke, M., Jugo, P.J., Klimm, K., Susini, J., Botcharnikov, R., Kohn, S.C., and Janousch, M. (2008) The origin of S^{4+} detected in silicate glasses by XANES. American Mineralogist, 93(1), 235–240.
Zhang, H.L., Solheid, P.A., Lange, R.A., von der Handt, A., and Hirschmann, M.M. (2015) Accurate determination of $Fe^{3+}/\Sigma Fe$ of andesitic glass by Mössbauer spectroscopy. American Mineralogist, 100(8-9), 1967–1977.
Zhang, H.L., Hirschmann, M.M., Cottrell, E., Newville, M., and Lanzirotti, A. (2016) Structural environment of iron and accurate determination of $Fe^{3+}/\Sigma Fe$ ratios in andesitic glasses by XANES and Mössbauer spectroscopy. Chemical Geology, 428, 48–58.
Zhang, H.L., Cottrell, E., Hirschmann, M.M., and Kelley, K.A. (2018) Determination of $Fe^{3+}/\Sigma Fe$ of XANES basaltic glass standards by Mössbauer spectroscopy and its application to the oxidation state of iron in MORB. Chemical Geology, 479, 166–175.

Manuscript received August 4, 2017
Manuscript accepted January 9, 2018
Manuscript handled by Sasa Bajt

Endnote:

[1]Deposit item AM-18-46268, Supplemental Material and Figures. Deposit items are free to all readers and found on the MSA web site, via the specific issue's Table of Contents (go to http://www.minsocam.org/MSA/AmMin/TOC/2018/Apr2018_data/Apr2018_data.html).